

Increasing the Spatial Resolution and Sensitivity of Magnetic Resonance Elastography by Correcting for Subject Motion and Susceptibility-Induced Image Distortions

Andreas Fehlner, PhD,¹ Sebastian Hirsch, PhD,² Martin Weygandt, PhD,^{3,4}
 Thomas Christophel, PhD,^{3,4} Eric Barnhill, PhD,¹ Mykola Kadobianskyi, MS,^{3,4}
 Jürgen Braun, PhD,² Johannes Bernarding, PhD,⁵
 Ralf Lützkendorf, Diplomingenieur,⁵ Ingolf Sack, PhD,¹ and Stefan Hetzer, PhD^{3,4*}

Purpose: To improve the resolution of elasticity maps by adapting motion and distortion correction methods for phase-based magnetic resonance imaging (MRI) contrasts such as magnetic resonance elastography (MRE), a technique for measuring mechanical tissue properties in vivo.

Materials and Methods: MRE data of the brain were acquired with echo-planar imaging (EPI) at 3T ($n = 14$) and 7T ($n = 18$). Motion and distortion correction parameters were estimated using the magnitude images. The real and imaginary part of the complex MRE data were corrected separately and recombined. The width of the point-spread function (PSF) and the position variability were calculated. The images were normalized to the Montreal Neurological Institute (MNI) anatomical template. The gray-to-white matter separability of the elasticity maps was tested.

Results: Motion correction sharpened the $|G^*|$ maps as demonstrated by a narrowing of the PSF by 0.78 ± 0.51 mm at 7T and 0.52 ± 0.63 mm at 3T. The amount of individual head motion during MRE acquisition correlated with the decrease in the width of the PSF at 7T ($r = 0.53$, $P = 0.025$) and at 3T ($r = 0.69$, $P = 0.006$) and with the increase of gray-to-white matter separability after motion correction at 7T ($r = 0.64$, $P = 0.0039$) and at 3T ($r = 0.57$, $P = 0.0319$). Improved spatial accuracy after distortion correction results in a significant increase in separability of gray and white matter stiffness ($P = 0.0067$), especially in inferior parts of the brain suffering from strong B_0 inhomogeneities.

Conclusion: We demonstrate that our method leads to sharper images and higher spatial accuracy, raising the prospect of the investigation of smaller brain areas with increased sensitivity in studies using MRE.

Level of Evidence: 1

Technical Efficacy: Stage 1

J. MAGN. RESON. IMAGING 2017;46:134–141

Magnetic resonance elastography (MRE) is a phase-based imaging modality that allows measurements of viscoelastic tissue properties in vivo.¹ MRE propagates mechanical waves into the body in order to investigate subtle variations of viscoelasticity in the spatial² or temporal

domain.³ This technique has been successfully applied in studies of different neurological disorders, such as multiple sclerosis,⁴ Parkinson's disease,⁵ amyotrophic lateral sclerosis,⁶ dementia,⁷ as well as brain tumors.⁸ Recent developments towards high-resolution multifrequency MRE at higher field

View this article online at wileyonlinelibrary.com. DOI: 10.1002/jmri.25516

Received Jul 31, 2016, Accepted for publication Oct 5, 2016.

*Address reprint requests to: S.H., Berlin Center for Advanced Neuroimaging, Charitéplatz 1, 10117 Berlin, Germany. E-mail: stefan.hetzer@charite.de

From the ¹Department of Radiology, Charité – Universitätsmedizin Berlin, Berlin, Germany; ²Institute of Medical Informatics, Charité – Universitätsmedizin Berlin, Berlin, Germany; ³Berlin Center for Advanced Neuroimaging, Charité – Universitätsmedizin Berlin, Berlin, Germany; ⁴Bernstein Center for Computational Neuroscience, Berlin, Germany; and ⁵Institute of Biometry and Medical Informatics, Otto-von-Guericke University, Magdeburg, Germany

The first two authors contributed equally to this work.

strengths enable the investigation of small areas within the brain but require correction for artifacts of the MRE measurement process, significantly impairing the spatial precision. In this study we addressed two sources of error of spatial precision for high-resolution MRE: Subject motion during the measurement process and echo-planar imaging (EPI) distortions caused by susceptibility-induced B_0 inhomogeneities.

Subject motion during data acquisition can be in the range of several millimeters, resulting in blurring and more complex image artifacts for segmented sequences.

Different approaches for motion correction have been developed for various MRI applications. In prospective motion correction, the imaging gradients are adjusted in real time based on rigid-body motion parameters extracted from the MRI data stream, e.g., *k*-space navigators⁹ or image-based navigators,¹⁰ or from external sensors, e.g., via active MR markers^{11,12} or via optical cameras.¹³ However, prospective motion correction is not yet widely available due to complexities of its technical implementation (e.g., calibration, modification of certified MR sequences) and reduced patient comfort in the case of the use of markers attached to the head.¹⁴

EPI is the most widely used MR sequence for the acquisition of dynamic series because of its capability to acquire an image within a few milliseconds, leading to a higher signal-to-noise efficiency (SNR per measurement time) than most other MRI sequences.¹⁵ In contrast to segmented MR sequences, in the scope of this work subject motion during the acquisition of a single image is assumed to be negligible for single-shot EPI, and motion correction can thus be performed retrospectively by employing rigid-body transformations to align all brain volumes of a time series to a reference volume during postprocessing.

Because of its acquisition speed, EPI is widely used in MRE to acquire the underlying wave field images. However, EPI is susceptible to image distortions caused by local susceptibility-induced B_0 inhomogeneities. These distortions scale with image resolution and field strength.¹⁶ It is well known that correcting for EPI distortions improves the anatomical localization, thus significantly increasing the statistical power of multisubject studies.¹⁷

However, existing pipelines for motion and distortion correction consider magnitude images only and need to be adapted for phase-based contrasts. In this work we present and assess a novel processing pipeline and analyze the increase of spatial specificity—on the example of MRE. By employing well-established algorithms for motion and distortion correction, improvements of the adapted pipeline are quantified on MRE data acquired at 3T and 7T.

Materials and Methods

Subjects

Two groups of healthy volunteers were investigated at 3T ($n = 14$) and 7T ($n = 18$) using multifrequency MRE. The study was

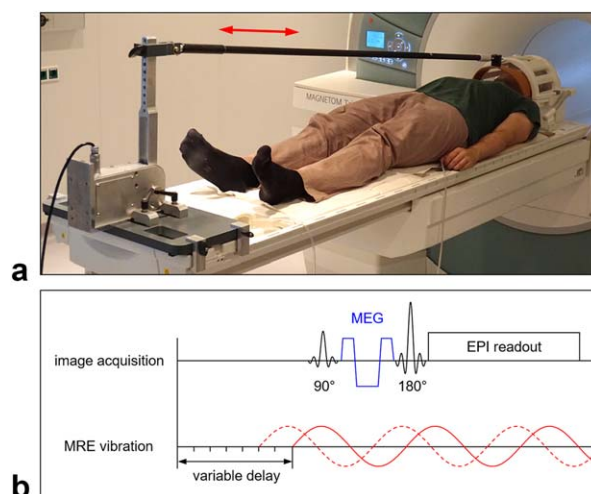


FIGURE 1: a: Technical MRE setup in a 3T scanner with the actuator transferring mechanical vibrations to the head. **b:** Images of the corresponding wave fields are acquired with a spin echo EPI sequence equipped with three orthogonal motion encoding gradients (MEG) that store the tissue displacement information in the phase of the complex-valued EPI images. In order to sample the dynamics of the time-harmonic wave propagation a variable delay is introduced covering eight points of one wave period.

approved by the Ethics Committees of the Charité – Universitätsmedizin Berlin and of the Otto-von-Guericke-University Magdeburg in conformity with the Declaration of Helsinki. All study participants gave written informed consent prior to the examination.

Image Acquisition

Experiments were performed on whole-body MRI scanners (Siemens Healthcare, Erlangen, Germany) at 7T (Magnetom 7T, software version VB17UHF) equipped with a 70 mT/m gradient coil and a 32-channel head coil (Nova Medical, Wakefield, MA), and at 3T (Magnetom Trio, software version VB17A) equipped with a 45 mT/m gradient coil and the standard 12-channel head coil.

MRE was performed utilizing a head cradle actuator connected to a piezo-electrical vibration generator (Fig. 1a) as detailed previously.⁴ A single-shot spin-echo EPI sequence, with trapezoidal flow-compensated motion-encoding gradients (MEGs) was used to acquire MRE images at three mechanical drive frequencies (30 Hz, 40 Hz, 50 Hz) with eight acquisitions over one wave cycle and three orthogonal motion encoding gradients (Fig. 1b) resulting in a series of 72 volumes acquired within 10 minutes.

At 3T, 2 mm isotropic resolution was achieved with 40 transversal slices covering the whole brain with a matrix size of 88×100 , echo spacing 0.72 msec, echo time (TE) = 82 msec, repetition time (TR) = 8.5 sec. At 7T high-resolution MRE data of 1 mm isotropic resolution were acquired with 42 transversal slices covering the superior part of the brain with a matrix size of 200×200 , echo spacing 1.08 msec, TE = 76 msec, TR = 8.3 sec. All EPI series were acquired with phase-encoding direction from right to left (R→L).

For distortion correction, two EPI reference volumes with opposite phase-encoding directions (R→L and L→R) were acquired with exactly the same imaging parameters as the

corresponding MRE EPI series but without vibrations and motion-encoding gradients. Additionally, an MPRAGE scan with 1 mm isotropic resolution was acquired for anatomical reference.

Processing Pipeline

Image processing was performed using MatLab (MathWorks, Natick, MA), and standard software packages designed for the analysis of brain imaging data: Statistical Parametric Mapping (SPM v. 12, Wellcome Trust Centre for Neuroimaging, London, UK) and the FMRI Software Library (FSL v. 5, Oxford Centre for Functional MRI of the Brain, Oxford, UK).

Both distortion and motion correction can be formulated as linear operations on complex MRE data. However, the above-mentioned tools that were used to perform these steps were implemented specifically for real-valued data and cannot cope with complex data. Correction of the phase directly is not possible, as the defining property of linear operators L , that for any complex number $z = a + i \cdot b$,

$$L(a + i \cdot b) = L(a) + i \cdot L(b),$$

is not applicable to the parameterization $z = |z| \cdot e^{i\phi}$. Consequently, we separate the complex data into real and imaginary parts, perform the corrections on these separately, and then reconstruct the corrected image phase from the corrected real and imaginary part according to:

$$\phi_{corr} = \arctan\left(\frac{b_{corr}}{a_{corr}}\right).$$

Subject motion parameters were first calculated with the SPM realign routine, estimating the rigid-body spatial transformation (rotation and translation) by minimizing the sum of squared differences between each MRE magnitude volume and the corresponding EPI reference volume.

Second, for the correction of geometric distortion induced by B_0 inhomogeneities, the *FSL-Topup* tool¹⁸ was used to estimate a B_0 offset map from two reference volumes that were acquired with opposite phase-encode blips, and so had distortions in opposite directions. This B_0 map was then used to undistort all MRE volumes by applying the algorithm described previously.¹⁹

The corrected MRE series were processed by a multifrequency MRE processing pipeline to generate high-resolution maps of viscoelastic properties as outlined previously.²⁰ In short, high-resolution elastograms were obtained after the following steps: 1) Gradient unwrapping²¹ after 2D Gaussian denoising with 5 pixel edge size and $\sigma = 0.65$ provides derivative components (two in-plane derivatives for each field component, through-plane derivatives had to be discarded due to phase discontinuities between slices²²). 2) Temporal Fourier transformation to generate six complex-valued wave derivative images. 3) Noise suppression by a 2D Butterworth lowpass filter with a threshold of 100 m^{-1} . 4) Multifrequency dual elasto-visco inversion (MDEV). MDEV inversion provides high-resolution maps of the magnitude of the complex shear modulus G^* ,²³ quantifying tissue stiffness.

In order to analyze the relationship between the increase in image sharpness after motion correction and the individual extent

of motion beyond subjective visual inspection, the image sharpness was quantified by estimating the full width at half maximum (FWHM) of the point-spread function (PSF) of the MRE process with *FSL-smoothest*,²⁴ which estimates the FWHM of the Gaussian kernel required to smooth uncorrelated white noise data to have the same inherent spatial correlation among adjacent voxels as the analyzed MRE data. The individual extent of motion during the MRE acquisition was quantified by calculating the position variability:

$$PV = s2 \sqrt{\left(\frac{1}{3} \sum_{i=x,y,z} \sigma(T_i)\right)^2 + \left(\frac{1}{3} \sum_{i=\alpha,\beta,\gamma} \sigma(R_i)\right)^2}$$

from the standard deviations σ of the six rigid-body realignment parameters (translation $T_{x,y,z}$; rotation $R_{\alpha,\beta,\gamma}$) after converting rotational displacements R_i from degrees to millimeters.²⁵

Finally, the combined spatial normalization and segmentation algorithm included in SPM was employed to spatially coregister the MRE data to the individual MPRAGE scan and to the anatomical standard space, respectively, as defined by the Montreal Neurological Institute (MNI) brain template.²⁶ Specifically, in this procedure the algorithm generated individual tissue probability maps (TPM) for white matter (WM), gray matter (GM), and cerebrospinal fluid (CSF) as well as deformation fields D_x , D_y , D_z that represent the nonlinear parts of the spatial transformation applied during image coregistration.

Statistical Analysis

All statistical analyses were performed using the MatLab Statistics Toolbox. A P -value < 0.05 was considered statistically significant for all statistical tests.

The influence of the *motion* correction on the separability of stiffness in gray matter and white matter was tested by correlating across subjects the change of t -values from two Student's t -tests between gray and white matter voxels with and without motion correction ($t_{corr} - t_{uncorr}$) for each brain calculated across all gray and white matter voxels as classified by the corresponding TPMs) with the PV values for the individual subjects.

We quantified the general impact of *distortion* correction on the accuracy of the normalization to MNI space. For this, we correlated the individual tissue masks (for GM, WM, and CSF) of the distorted and undistorted EPI images with the standard brain template tissue probability masks.

We then analyzed whether the gray-to-white matter separability of the elasticity maps was improved by the distortion correction. For this, we first calculated t -values within each subject for maps with and without distortion correction that reflected the stiffness difference between gray and white matter for the whole brain. We then calculated a paired one-sided t -test across subjects between these t -values calculated within each subject ($t_{corr} - t_{uncorr}$).

Finally, we tested whether the distortion correction resulted in a greater contrast improvement in parts of the image that showed stronger distortion (corresponding to higher B_0 inhomogeneity). For this, we correlated across slices the magnitude of the B_0 field with the improvement of separation ($t_{corr} - t_{uncorr}$) of the stiffness values in GM and WM. To test these individual subject

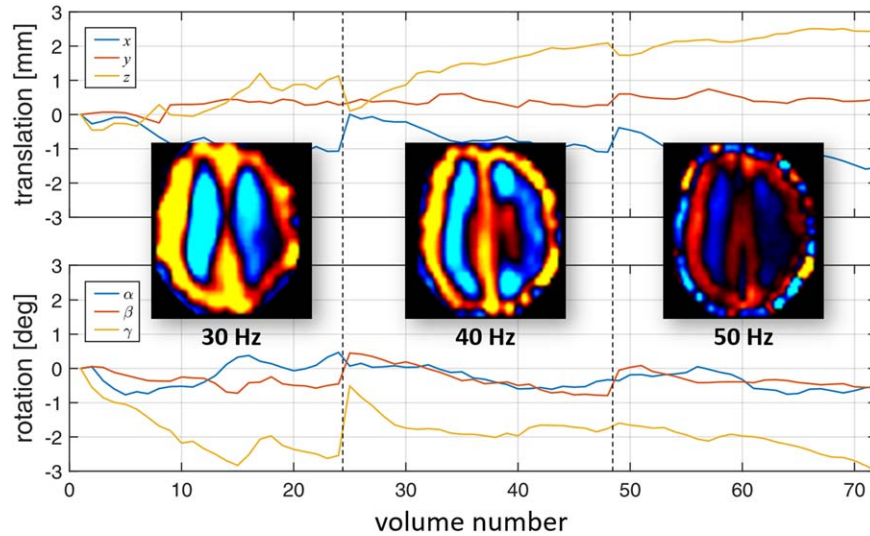


FIGURE 2: Rigid-body motion parameters of one MRE series for one subject with vertical dashed lines indicating when the driving frequency is switched between 30 Hz, 40 Hz, and 50 Hz. The wave fields corresponding to each driving frequency are shown as an overlay illustrating the decrease of wavelength at higher excitation frequency.

correlations at the group level, the correlation coefficients were converted to z -values using Fisher's r -to- z transform. These individual-subject z -values were used in a one-sample t -test (thresholded at $P < 0.05$).

Results

The volunteer cohorts consisted of 14 subjects (men only, mean age \pm standard deviation, 37 ± 12 years, range, 20–56 years) at 3T and 18 subjects (14 men, mean age, 35 ± 11 years, range 24–62 years) at 7T.

Motion Correction

Figure 2 shows the rigid-body motion parameters of one subject measured at 7T with above-average motion (position

variability, $PV = 1.7$ mm). Figure 3a shows the corresponding MRE data before and after motion correction. Due to the small isotropic voxels size of 1 mm enabled by measurement at 7T, the increase of sharpness is visually perceivable for both the magnitude image and the corresponding viscoelasticity map (Fig. 3a).

For all subjects, correction of subject motion reduced the FWHM of the PSF by 0.78 ± 0.51 mm for the 7T data, and by 0.52 ± 0.63 mm for the 3T data.

The extent of motion, as quantified by PV, averaged over all subjects, was 0.85 ± 0.31 mm (7T) and 0.77 ± 0.23 mm (3T), respectively. A significant linear correlation between the individual PV-values and the FWHM-reduction of the PSF was found for both field strengths,

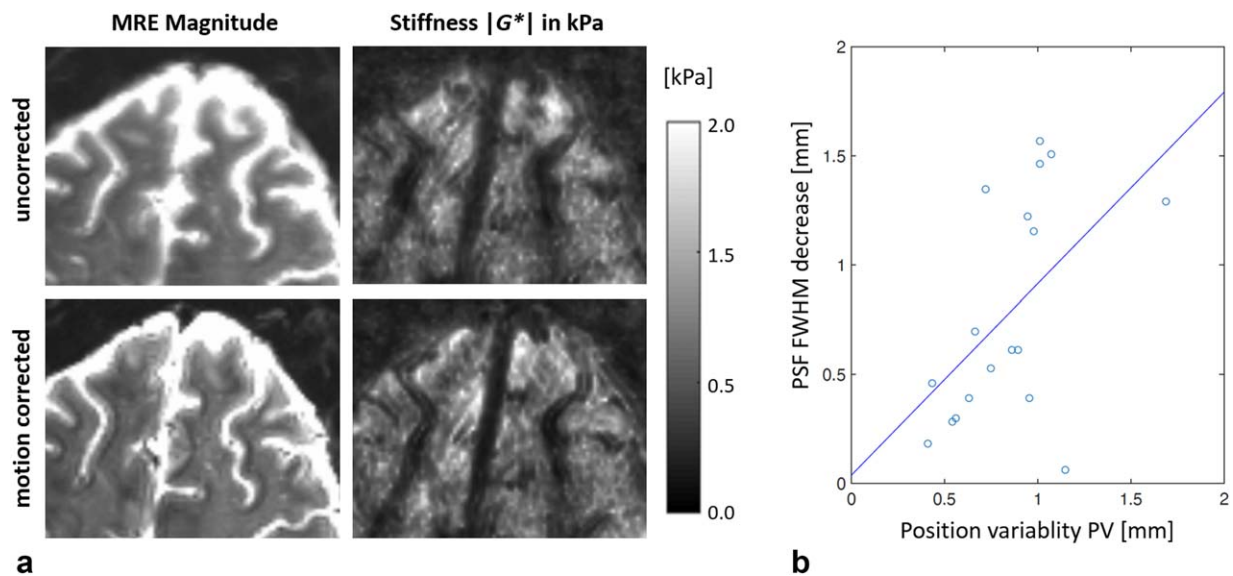


FIGURE 3: Motion-corrected MRE at 7T. **a:** The high spatial resolution of 1 mm isotropic voxels reveals the significantly sharper point-spread function (PSF) after motion correction (FWHM reduced by 1.3 mm in the lower images). **b:** Correlation between PV and the PSF FWHM decrease.

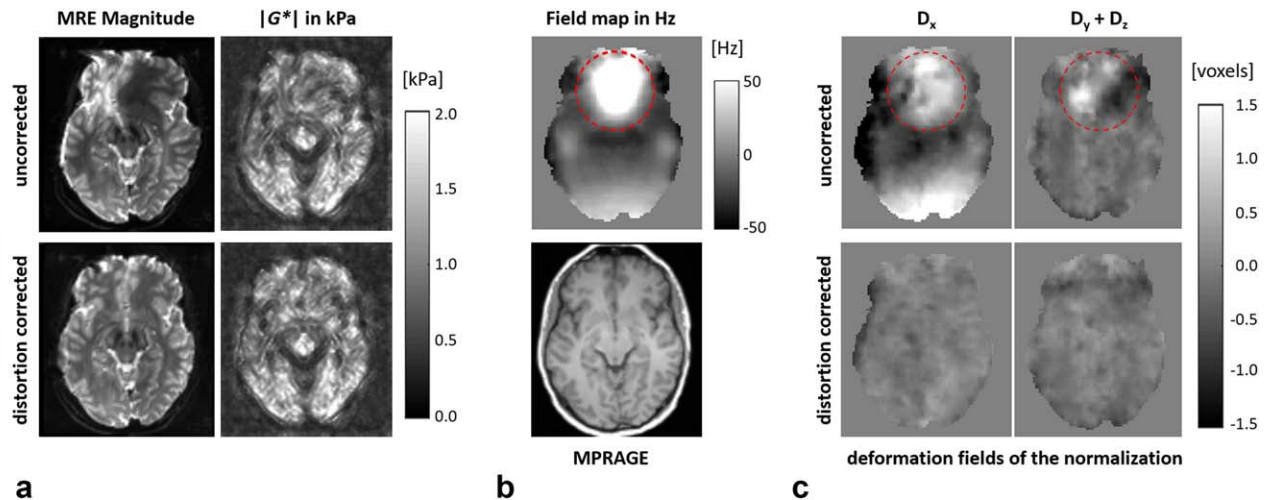


FIGURE 4: a: Example of increased spatial accuracy after correcting for distortions, shown in a single subject measured at 3T, in areas with strong B_0 inhomogeneities (b). c: Deformation fields (D_x in the phase-encoding direction) for the spatial normalization of the MRE magnitude image to the individual MPAGE. After distortion correction the deformations decrease to noise level.

with $r = 0.53$ ($P = 0.025$) at 7T and $r = 0.69$ ($P = 0.006$) at 3T (Fig. 3b).

A significant positive correlation between the individual PV-values and the increase ($t_{corr} - t_{uncorr}$) of GM/WM separation based on the t -statistics of the t -test was found for the high-resolution data acquired at 7T with ($r = 0.64$, $P = 0.0039$) and at 3T with ($r = 0.57$, $P = 0.0319$).

Distortion Correction

The increase of spatial accuracy after distortion correction is shown in Fig. 4a for regions with strong B_0 inhomogeneities in a subject measured at 3T. Among all three deformation field components extracted as the nonlinear part of the SPM normalization, the D_x component (in the phase-encoding direction) exhibits the highest amplitude. After distortion correction, all deformation maps decrease to noise level (Fig. 4c), reflecting the fact that the normalization without distortion correction is not capable of recovering the true anatomy.

For the 3T whole-brain data, in caudal brain parts that exhibit stronger B_0 inhomogeneities, we observed a 6% increase in correlation between the respective tissue masks and the corresponding standard TPM in MNI space (Fig. 5). The increase of correlation (Fig. 5b) significantly follows the course of the slice-wise averaged B_0 (Fig. 5c), with $r = 0.87$, $P < 0.001$. This increased spatial accuracy results in a significantly increased separation of GM and WM based on the viscoelasticity map $|G^*|$ after distortion correction (one-sided paired t -test between individual-subject t_{corr} and t_{uncorr} ; $P = 0.0067$). Furthermore, the increase in GM/WM separation significantly follows the variation of B_0 (correlation calculated across slices) as indicated by a group-level one-sample t -test ($t = 2.99$; $P = 0.0103$) on Fisher's z -transformed individual correlation coefficients ($r = 0.190 \pm 0.062$ SEM).

For the 7T data covering only the superior part of the brain with minimal B_0 inhomogeneities (gray box in Fig. 5b,c), no significant effects of the distortion correction were detected. In particular, no significant change of correlation between individual and standard MNI TPMs was found, and no dependence on the slice-wise averaged B_0 was

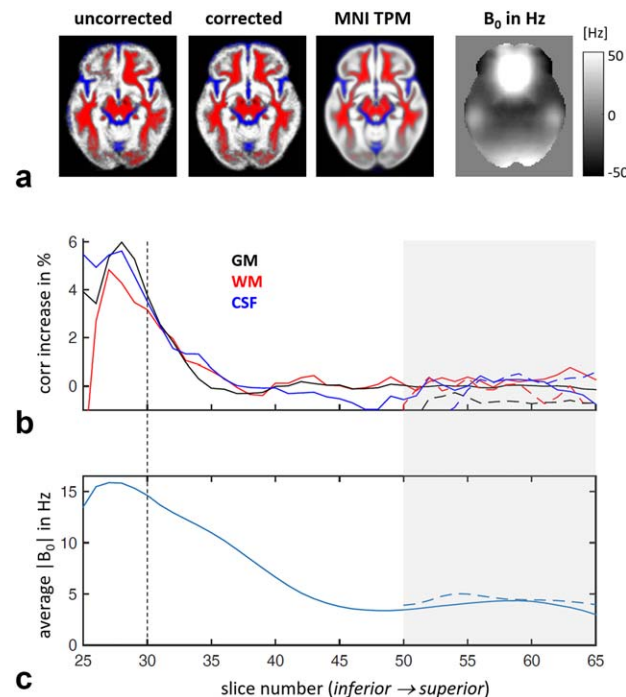


FIGURE 5: a: One exemplary slice (#30) with the tissue masks in MNI space (averaged over all subjects measured at 3T), the corresponding standard tissue probability maps (TPM) and the averaged B_0 . The increase of correlation (b) correlates positively with the course of the slice-wise averaged B_0 (c) with $r = 0.87$, $P < 0.001$. No such effect was observed for 7T data (represented by the dashed curves) covering only the superior part of the brain (gray box) with minimal distortions ($r = -0.02$, $P = 0.90$).

observed ($r = -0.02$; $P = 0.90$). Furthermore, there was no significant change in GM/WM separation of stiffness ($P = 0.93$).

Discussion

Our analysis confirmed that the correction of subject *motion* clearly sharpened the $|G^*|$ maps, which was demonstrated by a significant narrowing of the PSF. The amount of individual head motion during the MRE acquisition correlated with the decrease in the width of the PSF and with the increase of gray-to-white matter stiffness separability after motion correction.

Our retrospective approach corrects for the main source of motion—slow involuntary rigid-body movements of the head during a several-minute long measurement—while fast and rhythmic rigid-body displacements of the head due to breathing or heart pulsation are one order of magnitude smaller²⁷ than a typical voxel size. Because of the higher resolution achievable at 7T, small displacements have more adverse effects than at 3T. In contrast to multishot readouts²⁸ the effect of small phase errors induced by trajectory shifts during rigid-body motion can be neglected for single-shot EPI. More sophisticated prospective motion correction techniques might further improve the resulting image sharpness by correcting for rigid-body displacements unfolding in the subsecond domain, e.g., the aforementioned effects of breathing and heart pulsation or even potential effects of rigid-body vibrations transferred to the skull by the MRE actuator with a period smaller than a typical EPI slice readout time of a few tenths of a millisecond.

Furthermore, k -space navigator techniques correcting for dynamic nonlinear deformations could further increase the spatial resolution by correcting for deformations of brain tissue due to blood pulsation with displacement amplitudes⁹ around 100 μm that are one order of magnitude larger than the nonlinear deformations of the brain tissue due to the mechanical MRE shear waves with amplitudes around 10 μm .^{1,29}

Additionally, we report the use of *distortion* correction for MRE data and demonstrate that distortion correction enhanced the accuracy of normalization to the MNI space. This was demonstrated by an increase of the correlation between individual and standard MNI TPMs in regions with strong B_0 inhomogeneities. We interpret the reason for the increased accuracy of the normalization of the distortion-corrected images into MNI space as follows: EPI distortions occur exclusively along the phase-encode direction, whereas the nonrigid registration algorithm implemented by SPM allows for deformations along all directions. In the presence of large EPI distortions, the normalization algorithm finds a transform with significant deformations along the axes orthogonal to the phase-encoding direction, which ultimately leads to a distortion of

the true anatomy. Furthermore, it was shown that the improved spatial accuracy after distortion correction results in a significant increase in separability of GM and WM stiffness, especially in inferior parts of the brain suffering from strong B_0 inhomogeneities. It is expected that data acquired at higher field strengths is more heavily distorted and therefore would benefit more from distortion correction than data from lower field strengths for two reasons: First, B_0 inhomogeneities scale linearly with field strength.¹⁶ Second, higher spatial resolutions are achievable at higher field strength, leading to longer readout trains in single-shot sequences, resulting in more pronounced geometric distortions.

In our approach we followed the conventional assumption that the snapshot field map measured before the MRE acquisition is not significantly influenced by small rigid-body motion of the head.^{30,31} For this scenario, distortion correction can be performed either by measuring the field offset map directly by means of a dual-echo segmented sequence, or by the approach chosen for this work. In Ref. ¹⁸ it is shown that both approaches yield similar results; however, the EPI-based method is faster, with acquisition times of a few seconds vs. ~ 1 minute.

Respiration is not only a source of aforementioned small rigid-body motion of the head but it also distorts EPI images through perturbations of the static magnetic field B_0 over the brain caused by alterations of air-filled lung volume during the respiration cycle because air has significantly different magnetic susceptibility than tissue.³² Thus, especially at higher field strength, the spatial precision of MRE might further increase when time-efficient dynamic field mapping approaches^{33,34} can be used without interfering with phase modulations induced by the MRE wave patterns.

In general, all available inversion methods for the reconstruction of MRE parameters would benefit from motion and distortion correction. Generally speaking, the more data is combined into parameter reconstruction, the more attention should be paid to consistency of the data. Therefore, multifrequency and multicomponent inversion, such as MDEV, would see the largest benefit from the proposed method. This effect is amplified by the fact that longer data acquisition increases the likelihood of motion artifacts.

Several limitations have to be mentioned that will be dealt with in future studies. The development of the correction pipeline was performed on data that were originally acquired with a different objective than that presented in this work. For the high-resolution MRE data of 1 mm isotropic resolution acquired at 7T, whole-brain coverage was infeasible due to prohibitively long acquisition times. These slices were placed in the superior part of the brain specifically to avoid geometric distortions, thus hampering a comparison of the impact of distortion correction with whole-brain data acquired at 3T. The analyses of these data

demonstrated that there was no adverse effect of distortion correction in regions that were not affected by B_0 inhomogeneities.

As mentioned above, the assumption made implicitly in this work that motion and distortion artifacts can be corrected separately is a simplification. Under this assumption, it was necessary to perform motion correction first, so that all acquired volumes were aligned with the reference scans that could then be used for distortion correction. In a more comprehensive model, movement-by-susceptibility interactions and other sources of geometric distortions such as respiration affect the inhomogeneity map, so that the induced voxel displacement maps can be adapted for increasing the spatial precision of MRE. Moreover, using a more refined motion model, e.g., by incorporating motion information from external detectors, could help to eliminate higher-order motion-induced errors. These effects were not corrected for in the current work and might constitute the objective of future research.

In conclusion, the retrospective correction methods for MRE introduced in this work will help to increase the spatial precision and sensitivity of multisubject studies analyzing tissue elasticity e.g., in small subcortical areas²⁹ and its subdivisions or even within cortical layers. Our approach is simple to implement and can be applied to any EPI measurements without the need for sequence modification. It can also easily be transferred to other phase-based neuroimaging techniques employing EPI, e.g., for flow imaging,^{35,36} susceptibility-weighted imaging,³⁷ or variants of diffusion-weighted imaging³⁸ and functional MRI^{39,40} that take the image phase into account. The distortion correction method was originally conceived for single-shot EPI data that by design suffers much more pronouncedly from B_0 inhomogeneities than segmented sequences. However, in principle the same algorithm is also applicable for data from segmented spin-echo acquisitions if geometric distortions are present, e.g., in the vicinity of metal implants.

Acknowledgments

Contract grant sponsor: Hanns Seidel Foundation (scholarship to A.F.); Contract grant sponsor: German Federal Ministry for Education and Research (BMBF); contract grant number: 01GQ1408 (to I.S.); Contract grant sponsor: German Research Foundation; contract grant number: Sa901/17 (to I.S.)

The authors thank Christian Labadie for fruitful discussions. MRI at 3T was performed at the Berlin Center for Advanced Neuroimaging.

References

1. Muthupillai R, Lomas DJ, Rossman PJ, Greenleaf JF, Manduca A, Ehman RL. Magnetic resonance elastography by direct visualization of propagating acoustic strain waves. *Science* 1995;269:1854–1857.

2. Braun J, Guo J, Lützkendorf R, et al. High-resolution mechanical imaging of the human brain by three-dimensional multifrequency magnetic resonance elastography at 7T. *NeuroImage* 2014;90:308–314.
3. Freimann FB, Streitberger K-J, Klatt D, et al. Alteration of brain viscoelasticity after shunt treatment in normal pressure hydrocephalus. *Neuroradiology* 2012;54:189–196.
4. Fehlnér A, Behrens JR, Streitberger K-J, et al. Higher-resolution MR elastography reveals early mechanical signatures of neuroinflammation in patients with clinically isolated syndrome. *J Magn Reson Imaging* 2016;44:51–58.
5. Lipp A, Trbojevic R, Paul F, et al. Cerebral magnetic resonance elastography in supranuclear palsy and idiopathic Parkinson's disease. *NeuroImage Clin* 2013;3:381–387.
6. Romano A, Guo J, Prokscha T, et al. In vivo waveguide elastography: effects of neurodegeneration in patients with amyotrophic lateral sclerosis. *Magn Reson Med* 2014;72:1755–1761.
7. Huston J, Murphy MC, Boeve BF, et al. Magnetic resonance elastography of frontotemporal dementia. *J Magn Reson Imaging* 2016;43:474–478.
8. Yin Z, Glaser KJ, Manduca A, et al. Slip interface imaging predicts tumor-brain adhesion in vestibular schwannomas. *Radiology* 2015;277:507–517.
9. Ward HA, Riederer SJ, Grimm RC, Ehman RL, Felmlee JP, Jack CR. Prospective multiaxial motion correction for fMRI. *Magn Reson Med* 2000;43:459–469.
10. Thesen S, Heid O, Mueller E, Schad LR. Prospective acquisition correction for head motion with image-based tracking for real-time fMRI. *Magn Reson Med* 2000;44:457–465.
11. Derbyshire JA, Wright GA, Henkelman RM, Hinks RS. Dynamic scan-plane tracking using MR position monitoring. *J Magn Reson Imaging* 1998;8:924–932.
12. Haeberlin M, Kasper L, Barmet C, et al. Real-time motion correction using gradient tones and head-mounted NMR field probes. *Magn Reson Med* 2015;74:647–660.
13. Zaitsev M, Dold C, Sakas G, Hennig J, Speck O. Magnetic resonance imaging of freely moving objects: prospective real-time motion correction using an external optical motion tracking system. *NeuroImage* 2006;31:1038–1050.
14. Maclaren J, Herbst M, Speck O, Zaitsev M. Prospective motion correction in brain imaging: a review. *Magn Reson Med* 2013;69:621–636.
15. Cohen MS, Weisskoff RM. Ultra-fast imaging. *Magn Reson Imaging* 1991;9:1–37.
16. Jezzard P, Balaban RS. Correction for geometric distortion in echo planar images from B_0 field variations. *Magn Reson Med* 1995;34:65–73.
17. Cusack R, Brett M, Osswald K. An evaluation of the use of magnetic field maps to undistort echo-planar images. *NeuroImage* 2003;18:127–142.
18. Andersson JLR, Skare S, Ashburner J. How to correct susceptibility distortions in spin-echo echo-planar images: application to diffusion tensor imaging. *NeuroImage* 2003;20:870–888.
19. Chang H, Fitzpatrick JM. A technique for accurate magnetic resonance imaging in the presence of field inhomogeneities. *IEEE Trans Med Imaging* 1992;11:319–329.
20. Streitberger K-J, Reiss-Zimmermann M, Freimann FB, et al. High-resolution mechanical imaging of glioblastoma by multifrequency magnetic resonance elastography. *PLoS One* 2014;9:e110588.
21. Papazoglou S, Xu C, Hamhaber U, et al. Scatter-based magnetic resonance elastography. *Phys Med Biol* 2009;54:2229–2241.
22. Murphy MC, Huston J, Glaser KJ, Manduca A, Felmlee JP, Ehman RL. Phase correction for interslice discontinuities in multislice EPI MR elastography. In: *Proc ISMRM*, Melbourne; 2012:3426.
23. Hirsch S, Guo J, Reiter R, et al. MR elastography of the liver and the spleen using a piezoelectric driver, single-shot wave-field acquisition, and multifrequency dual parameter reconstruction. *Magn Reson Med* 2014;71:267–277.

24. Worsley K. An unbiased estimator for the roughness of a multivariate Gaussian random field. Montreal: McGill University, 1996 .
25. Power JD, Barnes KA, Snyder AZ, Schlaggar BL, Petersen SE. Spurious but systematic correlations in functional connectivity MRI networks arise from subject motion. *NeuroImage* 2012;59:2142–2154.
26. Tzourio-Mazoyer N, Landeau B, Papathanassiou D, et al. Automated anatomical labeling of activations in SPM using a macroscopic anatomical parcellation of the MNI MRI single-subject brain. *NeuroImage* 2002;15:273–289.
27. Maclaren J, Armstrong BSR, Barrows RT, et al. Measurement and correction of microscopic head motion during magnetic resonance imaging of the brain. *PLoS One* 2012;7:e48088.
28. Johnson CL, Holtrop JL, McGarry MDJ, et al. 3D multislabs, multishot acquisition for fast, whole-brain MR elastography with high signal-to-noise efficiency. *Magn Reson Med* 2014;71:477–485.
29. Johnson CL, Schwarb H, D J McGarry M, et al. Viscoelasticity of sub-cortical gray matter structures. *Hum Brain Mapp* 2016 [Epub ahead of print]. doi:10.1002/hbm.23314.
30. Jezzard P, Clare S. Sources of distortion in functional MRI data. *Hum Brain Mapp* 1999;8:80–85.
31. Glasser MF, Sotiropoulos SN, Wilson JA, et al. The minimal preprocessing pipelines for the Human Connectome Project. *NeuroImage* 2013;80:105–124.
32. Van de Moortele P-F, Pfeuffer J, Glover GH, Ugurbil K, Hu X. Respiration-induced B0 fluctuations and their spatial distribution in the human brain at 7 Tesla. *Magn Reson Med* 2002;47:888–895.
33. Lamberton F, Delcroix N, Grenier D, Mazoyer B, Joliot M. A new EPI-based dynamic field mapping method: application to retrospective geometrical distortion corrections. *J Magn Reson Imaging* 2007;26:747–755.
34. Dymerska B, Poser BA, Barth M, Tractnig S, Robinson SD. A method for the dynamic correction of B0-related distortions in single-echo EPI at 7T. *NeuroImage* 2016 [Epub ahead of print]. doi:10.1016/j.neuroimage.2016.07.009.
35. Debatin JF, Leung DA, Wildermuth S, Botnar R, Felblinger J, McKinnon GC. Flow quantitation with echo-planar phase-contrast velocity mapping: in vitro and in vivo evaluation. *J Magn Reson Imaging* 1995;5:656–662.
36. Bleeker EJW, van Buchem MA, Webb AG, van Osch MJP. Phase-based arterial input function measurements for dynamic susceptibility contrast MRI. *Magn Reson Med* 2010;64:358–368.
37. Holdsworth SJ, Yeom KW, Moseley ME, Skare S. Fast susceptibility-weighted imaging with three-dimensional short-axis propeller (SAP)-echo-planar imaging. *J Magn Reson Imaging* 2015;41:1447–1453.
38. Eichner C, Cauley SF, Cohen-Adad J, et al. Real diffusion-weighted MRI enabling true signal averaging and increased diffusion contrast. *NeuroImage* 2015;122:373–384.
39. Rowe DB. Modeling both the magnitude and phase of complex-valued fMRI data. *NeuroImage* 2005;25:1310–1324.
40. Balla DZ, Sanchez-Panchuelo RM, Wharton SJ, et al. Functional quantitative susceptibility mapping (fQSM). *NeuroImage* 2014;100:112–124.